Mechanical and permeability properties of skeletal and sheet triply periodic minimal surface scaffolds in bone defect reconstruction

Alejandro Yánez [a,*], Alberto Cuadrado [a], Oscar Martel [a], María Paula Fiorucci [a], Sebastiaan Deviaene [b]

[a] *Department of Mechanical Engineering, University of Las Palmas de Gran Canaria, Spain*
[b] *Department of Biomedical Engineering, Instituto Tecnológico de Canarias, Spain*

A R T I C L E   I N F O

A B S T R A C T

Triply periodic minimal surface (TPMS) structures have proven to be suitable for biomorphic scaffold designs orientated towards bone ingrowth applications. In this work, different types of gyroid Ti-6Al-4V scaffolds (skeletal-TPMS-based and sheet-TMPS-based) have been designed and fabricated by laser powder bed fusion for the purposes of analysing them and clarifying which type of scaffolds could be the best option to use in bone defect repair. The compression and bending tests conducted demonstrated that the skeletal gyroid scaffolds were flexible enough to promote bone healing. On the other hand, the sheet gyroid scaffolds tested might be too rigid to promote optimal bone growth inside the scaffold. The torsional properties were acceptable for most of the scaffolds. The values of Darcian permeability for all the tested scaffolds seemed to promote bone rather than cartilage ingrowth.

1. Introduction

Porous biomaterials obtained through additive manufacturing are viable and highly suitable in bone replacements [1]. Among the different causes of bone substitution, those that are *a priori* more demanding from a mechanical and biological point of view are the related to the large segmental bone defects. These defects can appear in long bones such as femur, tibia, fibula, humerus, etc. Although in the majority of those bones, the most critical loads are compression loads, in some other of the mentioned bones, flexion and/or torsion loads are also significant. Due to the high mechanical demands placed on those bones, porous metallic biomaterials have been postulated as one of the best solutions for large bone defects and the Ti-6Al-4V alloy has been sufficiently studied and verified to be efficient for this purpose [2]. One type of porous metallic biomaterials, which has proven to be suitable for bone replacements, is the triply periodic minimal surface (TPMS) scaffold.

Several additive manufacturing technologies work with Ti-6Al-4V, and the most developed ones are electron beam powder bed fusion (more commonly known as electron beam melting, EBM), and laser powder bed fusion (LPBF). There are many advantages and disadvantages of one technology over the other [3,4]. However, due to the large number of different companies that have developed LPBF technology,

there are numerous studies of bone scaffolds that have used said technology.

In the literature, only a few authors have analysed load applied to TPMS metallic scaffolds for bone substitute apart from compression, such as torsion or bending [5,6]. These features are the starting conditions for the choice of cell shape, pore size and strut size of scaffolds, variables that determine the porosity of the scaffolds.

The goal of the scaffolds presented in this study is to withstand load bearing while allowing the bone ingrowth. To that purpose, porosity plays a paramount role because the pores are the voids where the bone cells must grow, and they need an adequate mechanical environment. However, the mass transportation properties through the scaffold are critical too because it is necessary for the cells to transport nutrients and oxygen to them and to remove the waste that they generate [7,8]. Porosity alone cannot guarantee this feature, so to evaluate the mass transportation ability, permeability seems to be a good parameter [9]. Moreover, it has been suggested that higher permeability scaffolds promote bone regeneration and that increasing the permeability favours the bone growth against the cartilage formation [8,10,11].

In the recent literature, a large variety of TPMS structures (Primitive, I-WP, Diamond, Gyroid, Fischer Koch, etc.) of different metallic materials (Maraging steel, Ti-6Al-4V, Ni-Ti) has been studied [12–15]. TPMS

---

* Corresponding author.
E-mail address: alejandro.yanez@ulpgc.es (A. Yánez).

scaffolds have had great relevance in the field of bone regenerative medicine thanks to their good biomimetic and mechanical properties. There is still controversy to determine which is the best scaffolding from the mechanical and the biological point of view [16–18]. A certain consensus can be seen in the highlighting that both Diamond TPMS structures and Gyroid TPMS structures show good behaviour from the mechanical and the biological point of view [5,17,19]. AlMahri et al., 2021 [18] studied different TPMS lattice structures and found that the Diamond lattice structure exhibits the highest specific energy absorption value followed by the Gyroid, IWP, Fisher Koch and finally, the Primitive structure. However, Liu et al., 2020 [20] found that biological behaviour (higher cell density and higher osteoblast growth) was better in Gyroid structures than in Diamond structures. In this work, the study of the mechanical behaviour and permeability of different gyroid (skeletal and sheet) Ti-6Al-4 V scaffolds fabricated by LPBF was carried out.

Among the porous structures or scaffolds, two groups could be differentiated: the strut-based (or beam-based), and the TPMS-based. The major difference between them is that the strut-based scaffolds usually have straight uniform sections, whereas the TPMS-based structures do not. Concerning TPMS structures, it is possible to differentiate between two groups: the sheet-TPMS structures, which are created by offsetting the minimal surface along its normal direction to generate a double surface, and the solid-TPMS structures, also called skeletal-TPMS or skeleton-TPMS structures, depending on the authors, which are created considering the volume bound by the minimal surface [21]. Several studies compared skeletal and sheet TPMS structures focusing on compression properties. Al-Ketan et al., 2018 [12] found superior mechanical properties of sheet-TPMS versus solid-TPMS structures. Speirs et al., 2017 [22] investigated the mechanical properties of three different unit cells (octahedron, skeletal gyroid and sheet gyroid) of laser powder bed fusion nitinol scaffolds founding better static and fatigue behaviour of the TMPS structures (skeletal and sheet) versus the strut-based structure (octahedron). In all the cases mentioned above, only compression tests were carried out.

In this work, different types of gyroid scaffolds, both skeletal-TPMS-based structures and sheet-TMPS-based structures, were designed and fabricated by laser powder bed fusion for the purpose of analyzing the permeability and the mechanical properties under compression, flexion and torsion loads. The final goal is to clarify which type of scaffolds, skeletal-TPMS or sheet-TMPS, could be the best option to use as scaffolds in bone defect repair.

2. Materials and methods

2.1. Design and fabrication of scaffolds

Several porous structures or scaffolds (skeletal-TPMS, sheet-TPMS, and stochastic) were designed and fabricated by laser powder bed fusion (LPBF). Spherical Ti-6Al-4V ELI powder with a particle diameter in the range of 15–45 μm was used as raw material. The main fabrication parameters were a 320 W laser and a 60 μm layer thickness.

The fabricated scaffolds and their respective acronyms were: skeletal normal gyroid (SNG), skeletal deformed gyroid (SDG), skeletal normal gyroid with shell (SNGS), sheet gyroid 80 (SG80), sheet gyroid 70 (SG70), sheet gyroid 65 (SG65), sheet gyroid 80 drilled (SG80D), sheet gyroid 70 drilled (SG70D), sheet gyroid 65 drilled (SG65D) and stochastic scaffold (SS). They are shown in Fig. 1. Except for SG70, SG65, SG70D, and SG65D, the scaffolds were designed with a porosity close to 80 %. The description of the skeletal normal gyroid and that of the skeletal deformed gyroid have been described in previous works [6]. The SNGS scaffolds were similar to the SNG scaffolds but a small shell was added to the edges of the former to reinforce them and keep the same porosity and pore size. In the sheet gyroid scaffolds, the porosities and pore sizes were modified. Sheet gyroid drilled are like sheet gyroids that have had a series of drills/holes drilled into their walls. The

drills/holes consist of an array of spheres that match the periodicity of the gyroid surface. A diameter of 0.7 mm was chosen. The purpose of the drills/holes was, on the one hand, to allow the flow of fluid between both chambers, improving transversal permeability and, on the other hand, to try to make them more flexible.

The equations of the different TPMS scaffolds are shown as follows:

Sheet gyroid: $F(x, y, z) = \cos x \sin y + \cos y \sin z + \cos z \sin x + $ thickness factor (1)

Skeletal normal gyroid: $F(x, y, z) = \cos x \sin y + \cos y \sin z + \cos z \sin x + 0.05(\cos(2x)\cos(2y) + \cos(2y)\cos(2z) + \cos(2z)\cos(2x)) + $ thickness factor (2)

Skeletal deformed gyroid: $F(x, y, z) = \cos x \sin y + \cos y \sin(z/2) + \cos(z/2)\sin x + 0.05(\cos(2x)\cos(2y) + \cos(2y)\cos(2z) + \cos(2z)\cos(2x)) + $ thickness factor (3)

The unit cells of the different scaffolds were generated in K3Dsurf software (http://k3dsurf.sourceforge.net). They were then imported into 3D Studio Max software (Autodesk, Inc., United States) which, through custom-developed scripts, were used to fill the desired volume. Additional series of scripts and operators were developed to create anisotropic structures according to the required specifications.

Table 1 shows the theoretical strut/wall thickness and the pore size of the samples. The measurements have been obtained using MeshMixer software (Autodesk, Inc., United States).

2.2. Porosity

To obtain the apparent density, the structures were measured (obtaining the apparent volume) and weighed on a precision balance scale (50 g ± 0.01 g). All measurements were carried out at room temperature (20 ± 2 °C). The porosity P was calculated following Eq. (4),

$$P = (1 - \rho/\rho_0) \, 100 \, \%$$ (4)

where ρ is the apparent density and ρ_0 the bulk alloy density (4.42 g/cm^3).

2.3. Mechanical testing

Three different types of mechanical testing were conducted: uniaxial compression tests, bending tests and torsional tests. For those three mechanical tests, the number of tested samples for each type of scaffold was 3.

2.3.1. Uniaxial compression tests

The uniaxial compression tests were carried out following the international standard ISO 13314 [23]. Each test was conducted at a speed of 0.5 mm/min. In the testing machine (Microtest MEM-101/20A-SDC, Madrid, Spain), the upper head was articulated and the load was applied onto the plain plates placed on the upper and the lower sides of the specimens. Both stress and strain curves were obtained following the initial cross-sectional area and the initial length of each structure, respectively. The apparent Young modulus (E_{ap}) of each scaffold was obtained as the slope of the linear part of each stress-strain curve. The ultimate strength (σ_{max}) was obtained as the compressive stress corresponding to the first local maximum in the stress-strain curve.

2.3.2. Three-point bending tests

The three-point bending tests were carried out following the international standard ASTM C1674 [24] using the same material testing machine as mentioned in the previous section. The bending specimens had a prismatic shape with a square section. Bending samples are shown in Fig. 2. The dimensions as well as the supports spans from one of the samples are defined in Fig. 3. The samples were placed on the two
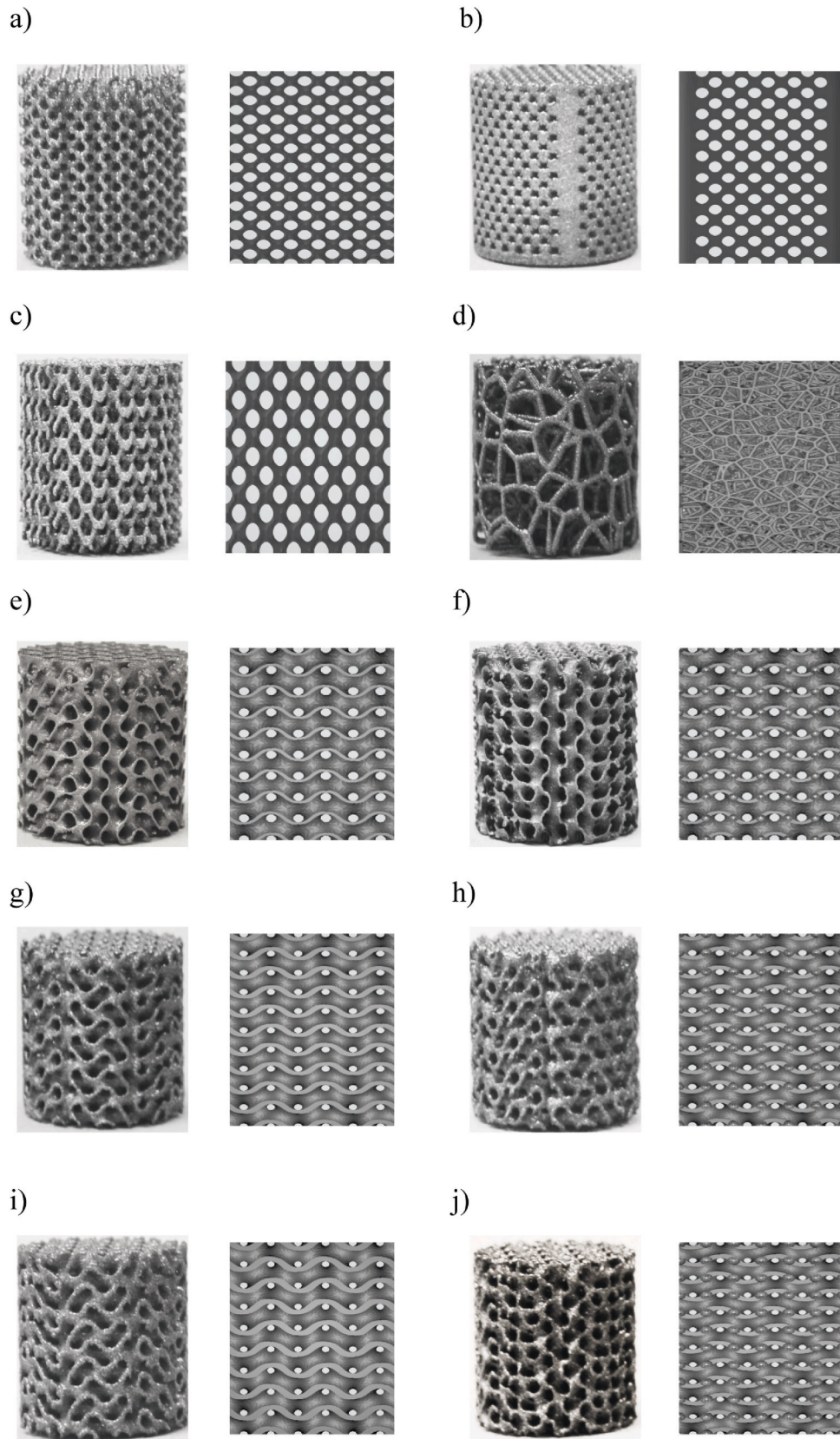
Fig. 1. Real pictures (left column) and CAD images (right column) of each of the scaffolds designed: a) skeletal normal gyroid (SNG), b) skeletal normal gyroid with shell (SNGS), c) skeletal deformed gyroid (SDG), d) stochastic structure (SS), e) sheet gyroid 80 (SG80), f) sheet gyroid 80 drilled (SG80D), g) sheet gyroid 70 (SG70), h) sheet gyroid 70 drilled (SG70D), i) sheet gyroid 65 (SG65), and j) sheet gyroid 65 drilled (SG65D).

Table 1

Theoretical strut and wall thickness and pore size of the porous Ti-6Al-4V scaffolds.

	Strut thickness for skeletal structures or wall thickness for sheet structures (mm)	Pore size (mm)
Skeletal normal gyroid	0.84	0.98
Skeletal normal gyroid with shell	0.85	0.98
Skeletal deformed gyroid	0.53	min 0.80 – max 1.60
Sheet gyroid 80	0.45	3.00
Sheet gyroid 70	0.45	1.10
Sheet gyroid 65	0.30	0.96
Sheet gyroid 80 drilled	0.30	3.00
Sheet gyroid 70 drilled	0.30	1.10
Sheet gyroid 65 drilled	0.30	0.96
Stochastic structure	0.83	–

supporting pins (down) and the load was applied by a third pin (up) placed in the middle of the two supporting pins. Each test was conducted at a speed of 0.5 mm/min.

The bending strength was calculated following Eq. (5),

$$\sigma_f = (3*F*L) / (2*a^3) \tag{5}$$

where F is the maximum load at a given point on the load deflection curve, L the support span and a the width of the specimen section. The apparent bending modulus (E_f) was calculated following Eq. (6):

$$E_f = (L^3 *m) / (4 * a^4) \tag{6}$$

where m is the slope of the initial straight-line portion of the load deflection curve. To quantify experimental error, three specimens of each type of scaffold were prepared for the three-point bending tests.

2.3.3. Torsional tests

The torsional tests were carried out following the international standard ASTM E 143 [25]. Torsion samples are shown in Fig. 4. In the machine used to perform the torsion tests, one of the grips was allowed free axial movement, thereby avoiding axial loads on the test specimens. Each test was conducted at a speed of 0.1 rad/min. The torques, including the torque to failure (T_{max}), and the angles were obtained from the slope of the torque–total angle of turn curve. Apparent shear modulus (G_{ap}) was calculated following Eq. (7):

$$G_{ap} = (T * L) / (J *\theta) \tag{7}$$

where T is the torque, L the gage length, J the polar moment of inertia of the section about its center, and θ the angle of twist, in radians. For a solid cylinder, J was calculated following Eq. (8).

$$J = \pi *·D^4 / 32 \tag{8}$$
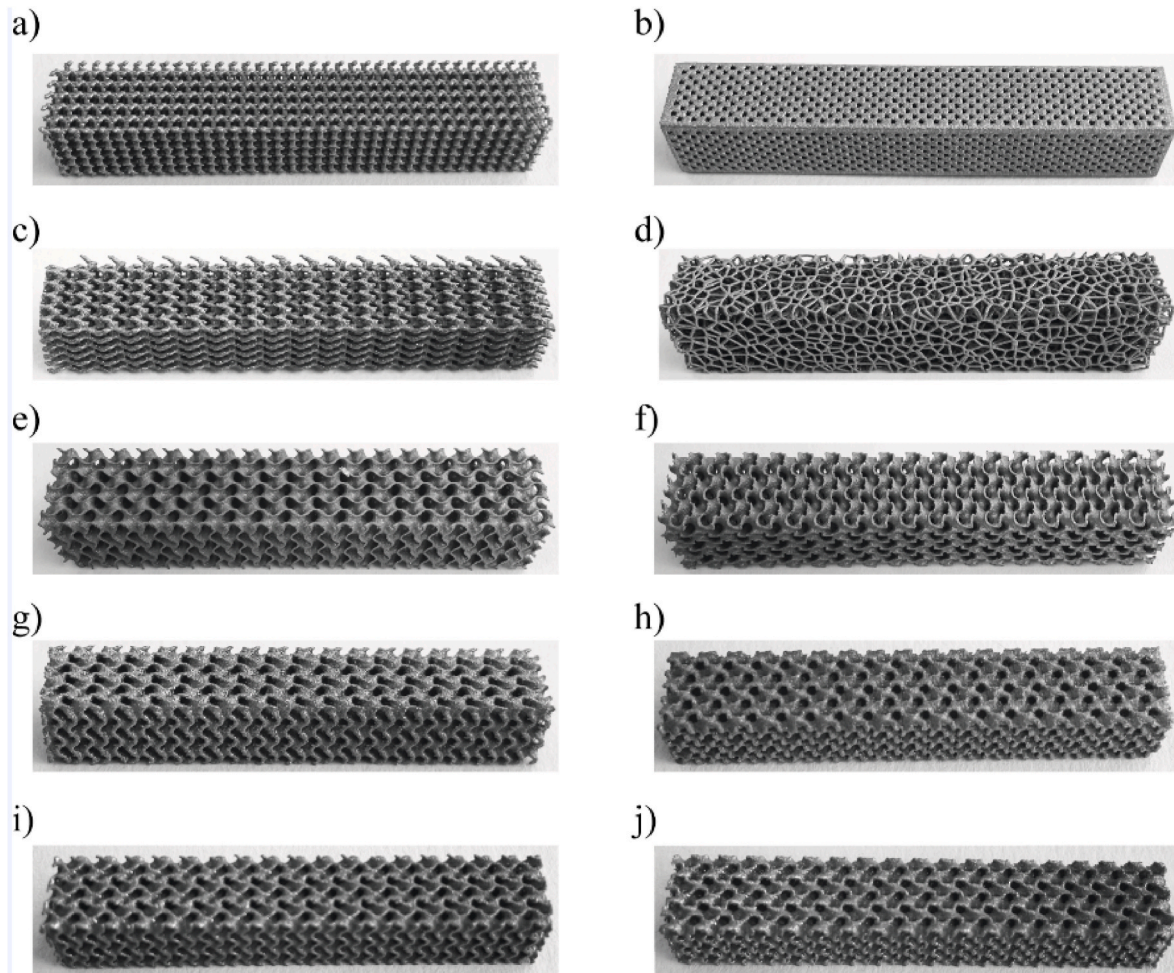
Fig. 2. Bending samples: a) skeletal normal gyroid (SNG), b) skeletal normal gyroid with shell (SNGS), c) skeletal deformed gyroid (SDG), d) stochastic structure (SS), e) sheet gyroid 80 (SG80), f) sheet gyroid 80 drilled (SG80D), g) sheet gyroid 70 (SG70), h) sheet gyroid 70 drilled (SG70D), i) sheet gyroid 65 (SG65), and j) sheet gyroid 65 drilled (SG65D).
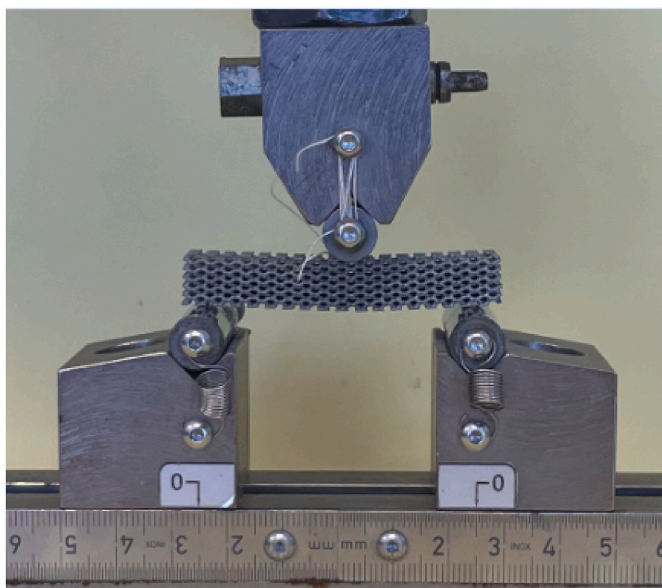
and the shear strength (τ_{max}) was calculated following Eq. (9).

$$\tau_{max} = T_{max} \cdot {}^* R / J \tag{9}$$

where *R* is the radius of the section.

Table 2 shows the dimensions of the bending and torsion samples.

2.4. Permeability measurements

The assessment of permeability depends on the type of behaviour

Fig. 3. Picture showing the three-point bending tests of the prismatic scaffold.

Table 2
Geometric parameters for bending and torsion tests.

|	Bending		Torsion	
	a (mm)	L (mm)	Ø (mm)	L (mm)
Skeletal Normal Gyroid (SNG)	12	50	13	48
Skeletal Normal Gyroid with Shell (SNGS)	12.60	50	13	47
Skeletal Deformed Gyroid (SDG)	9.75	50	10	39
Sheet Gyroid 80 (SG80)	24	100	25	96
Sheet Gyroid 70 (SG70)	9.50	40	9.50	38
Sheet Gyroid 65 (SG65)	8.50	40	8.35	31
Sheet Gyroid 80 Drilled (SG80D)	24	100	25	96
Sheet Gyroid 70 Drilled (SG70D)	9.50	40	9.50	38
Sheet Gyroid 65 Drilled (SG65D)	8.50	40	8.35	31
Stochastic Structure (SS)	25	100	25	99
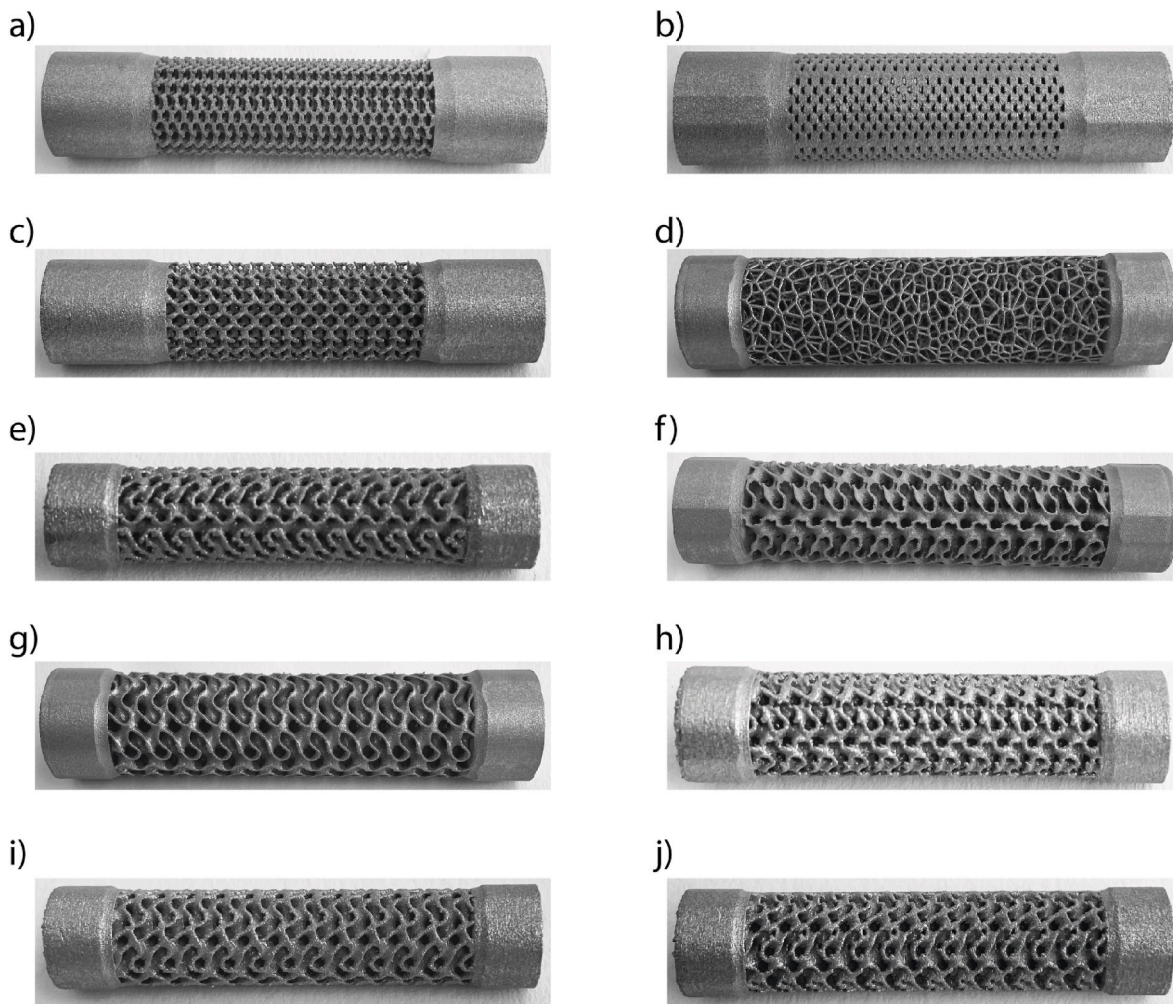
Fig. 4. Torsion samples: a) skeletal normal gyroid (SNG), b) skeletal normal gyroid with shell (SNGS), c) skeletal deformed gyroid (SDG), d) stochastic structure (SS), e) sheet gyroid 80 (SG80), f) sheet gyroid 80 drilled (SG80D), g) sheet gyroid 70 (SG70), h) sheet gyroid 70 drilled (SG70D), i) sheet gyroid 65 (SG65), and j) sheet gyroid 65 drilled (SG65D).

that the flow shows respect to the difference of pressure through the scaffold [26–28]. If the Reynold's number is low, the flow is considered to be laminar, the viscous effect dominates the flow, and the flow through the scaffold follows the Darcy's law (Eq. (10)). However, when the Reynold's number is high (usually Re > 10) the inertial effects of the flow are considerable and the Forchheimer's law (Eq. (11)) has shown good agreement to experimental data [7,29].

$$\Delta P = (\mu \ast L / K_D) \ast v \qquad (10)$$

$$\Delta P = (\mu \ast L / K_{DF}) \ast v + (\rho \ast L / K_{ND}) \ast v^2 \qquad (11)$$

In these equations v is the mean velocity of the fluid through the scaffold, μ the dynamic viscosity coefficient of the fluid, L the length of the scaffold over the fluid path, ΔP the pressure drop across the scaffold and ρ the density of the fluid. K_D is the Darcian permeability, K_{DF} the Darcian permeability when Forcheimer's law is applied and K_{ND} is the non-Darcian permeability.

With a custom-made apparatus, permeability was evaluated by using the gravity-based falling head method. The weight of the fluid W in the lower tank (Fig. 5) was measured with a scale and recorded on a time basis during all the tests. The volume V_O was obtained by dividing W by the specific weight of the fluid γ. The tests were started with water at an initial height H_I and stopped when water reached the final minimum level, H_F. Water flow was started and stopped by a ball valve. The pressure drop was $\Delta P = \rho \ast g \ast h$, where h is the height from the lower part of the scaffold to the free water surface in the upper tank. Finally, ΔP versus v could be plotted for each test (Fig. 6) and the three permeability coefficients previously defined could be obtained from the coefficients of the regression lines; the linear ones, representing Darcian

permeability and the quadratic one, representing non-Darcian permeability. Water at room temperature (20 °C) was used in all tests (n = 5).

Alternatively, another way to determine the Darcian permeability could be applying Eq. (12). To distinguish this permeability from the one calculated by the plot, this alternative one is referred to as $K\ast_D$. The main advantage of this calculation is its simplicity, since only the test time t_F must be calculated in each test.

$$K\ast_D = \ln (H_I / H_F) \ast (A_T \ast \mu \ast L) / (A_S \ast \rho \ast g \ast t_F) \qquad (12)$$

where A_T is the cross-sectional area of the upper tank and A_S the cross-sectional area of the scaffold.

Unpaired t-tests ($\alpha = 0.05$) were performed between the drilled and the non-drilled structures of the same type to assess drilling effect on permeability.

3. Results

3.1. Morphological analyses

Morphological parameters for different scaffolds were analysed. Table 3 shows the dry weighing porosity (mean and standard deviation values) for all the structures.

3.2. Mechanical properties: compression tests

Fig. 7 shows the compression mechanical properties of the different scaffolds. The highest values of both E_{ap} and σ_{max}, occurred in the sheet gyroid scaffold with the lowest porosity (3028.4 $\pm$ 47.5 and 185 $\pm$ 0.5 MPa, respectively). On the other hand, the lowest values of both E_{ap} and σ_{max} were found in the skeletal normal gyroid (953.5 $\pm$ 32.7 and 47.2 $\pm$ 2.2 MPa, respectively). In general, E_{ap} and σ_{max} values were higher in sheet gyroid scaffolds than in skeletal gyroid scaffolds. In the latter, both E_{ap} and σ_{max} values were increased by modifying the scaffold design: in one case, adding a shell to the scaffold (the skeletal normal gyroid with shell was 70 % stiffer and 62 % stronger than the skeletal normal gyroid), and in another case, elongating the cells in the direction of the load and obtaining ellipsoidal pores (the skeletal deformed gyroid was 81 % stiffer and 42 % stronger than the skeletal normal gyroid). In the sheet gyroids scaffolds, logically, both E_{qp} and σ_{max} values were inversely proportional to their porosities. With the drilling of holes in the walls of the sheet gyroid scaffolds, both E_{ap} and σ_{max} values decreased with respect to those which were not drilled. The sheet gyroid 80 was 5 % stiffer and 2 % stronger than the sheet gyroid 80 drilled; the sheet gyroid 70 was 26 % stiffer and 9 % stronger than the sheet gyroid 70 drilled; the sheet gyroid 65 was 17 % stiffer and 15 % stronger than the sheet gyroid 65 drilled. Both E_{ap} and σ_{max} values of the stochastic scaffold were low compared to the sheet gyroids (1001.2 $\pm$ 81.6 and 45.5 $\pm$ 3.1 MPa, respectively).

3.3. Bending mechanical properties

Fig. 8 shows the apparent bending modulus and the bending strength of the different scaffolds. As shown in compression tests, the maximum values of E_f and σ_f occurred in the sheet gyroid with the lowest porosity (4902.6 $\pm$ 157.6 and 313.6 $\pm$ 6.1 MPa, respectively), while the minimum values of both, E_f and σ_f, were for the skeletal normal gyroid (1136.3 $\pm$ 24.8 and 66.7 $\pm$ 2.4 MPa, respectively). The apparent bending modulus values were lower in the skeletal gyroid scaffolds than in the sheet gyroid ones, except for the normal gyroid with shell and skeletal deformed gyroids, which were stiffer than those of both the sheet gyroid 80 and the sheet gyroid 80 drilled. As for the bending tests, the skeletal normal gyroid with shell was 294 % stiffer and 178 % stronger than the skeletal normal gyroid, and the skeletal deformed gyroid was 99 % stiffer and 37 % stronger than the skeletal normal gyroid. In the sheet gyroid scaffolds, as in what happened in the
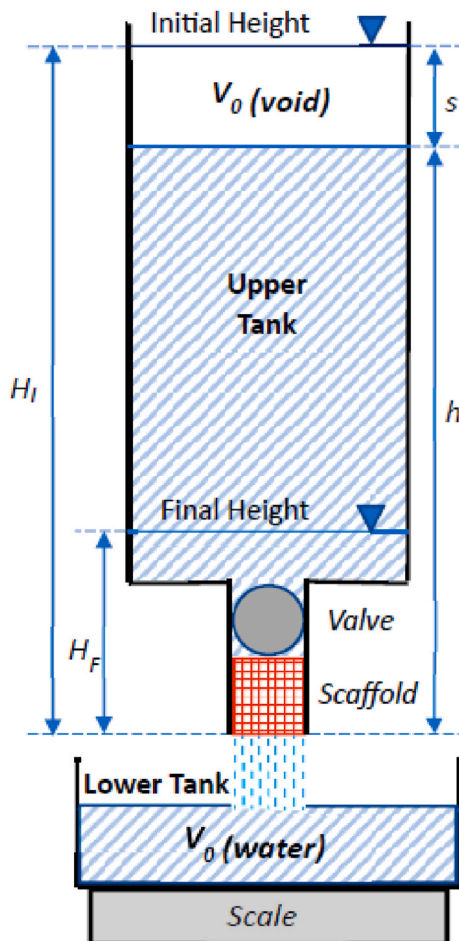

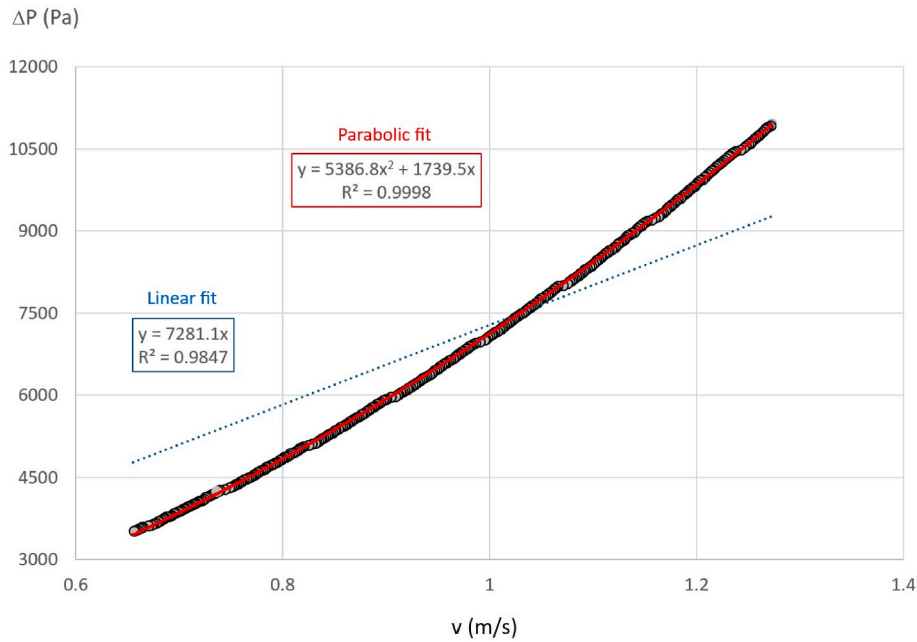**Fig. 5.** Schematic drawing of the falling head setup.

Fig. 6. ΔP vs. v for one of the tests of the skeletal deformed gyroid scaffolds. Linear (Darcy) and quadratic (Forchheimer) curve fit are shown along with their equations and coefficient of determination (R^2).

Table 3
Porosities of the porous Ti-6Al-4V scaffolds, given as means $\pm$ standard deviations.

	Dry weighing porosity (%)
Skeletal normal gyroid	77.94 ± 0.17
Skeletal normal gyroid with shell	NA
Skeletal deformed gyroid	81.06 ± 0.09
Sheet gyroid 80	79.83 ± 0.05
Sheet gyroid 70	68.16 ± 0.37
Sheet gyroid 65	63.15 ± 0.59
Sheet gyroid 80 drilled	80.70 ± 0.22
Sheet gyroid 70 drilled	71.44 ± 0.04
Sheet gyroid 65 drilled	67.66 ± 0.11
Stochastic structure	80.65 ± 0.01

compression tests, the E_f and σ_f values were inversely proportional to their porosities. Also, as verified in compression tests, the non-drilled sheet gyroid scaffolds were stiffer and stronger than the drilled ones. The sheet gyroid 80 was 34 % stiffer and 5 % stronger than the sheet gyroid 80 drilled; the sheet gyroid 70 was 31 % stiffer and 37 % stronger than the sheet gyroid 70 drilled; the sheet gyroid 65 was 24 % stiffer and 54 % stronger than the sheet gyroid 65 drilled.

3.4. Torsional mechanical properties

Fig. 9 shows the mechanical properties obtained from torsional tests (mean and standard deviation) of the scaffolds. The maximum G_{ap} and τ_{max} values occurred for the sheet gyroid 65 (5207.24 ± 34 MPa and 142.33 ± 0.78 MPa, respectively). The minimum G_{ap} value corresponded to the skeletal normal gyroid (851.52 ± 27.99 MPa). However, the minimum τ_{max} values occurred for the stochastic scaffolds (18.48 ± 0.66 MPa). In the skeletal normal gyroid with shell, both torsional stiffness and torsional strength increased significantly over the skeletal normal gyroid (497 % and 333 %, respectively). However, in the skeletal deformed gyroid concerning the skeletal normal gyroid, the increase in torsional stiffness and torsional strength was not as pronounced (20 % and 47 %, respectively). In the sheet gyroid scaffolds, the G_{ap} and τ_{max} values were inversely proportional to their porosities. In all porosities, the torsional stiffness and the torsional strength increased in the non-

drilled sheet gyroid scaffolds with respect to the drilled ones. The percentage differences in torsional stiffness and torsion strength, between non-drilled and drilled sheet gyroid scaffolds, increased with the decrease in porosity. The sheet gyroid 80 was 16 % stiffer and 17 % stronger than the sheet gyroid 80 drilled; the sheet gyroid 70 was 53 % stiffer and 45 % stronger than the sheet gyroid 70 drilled; the sheet gyroid 65 was 86 % stiffer and 73 % stronger than the sheet gyroid 65 drilled. Though the location was random, the type of torsional breakage that occurred in all the scaffolds was in 90° bands (Fig. 10). In some samples, the failure took place in the central area, whereas in other cases, the failure was closer to the clamps.

3.5. Permeability tests

Fluid velocity obtained in all scaffold tests ranged from 0.20 to 1.36 m/s leading to Reynold's number (Eq. (13)) between 200 and 1357, so the inertial effects are not negligible and Forchheimer's law fits very well the ΔP vs. v plot ($R^2 > 0.999$ in all tests). However, when fitting the curve to the linear model (Darcy) a $R^2 > 0.98$ was found in all cases.

$$Re = \rho * v * (pore\ diameter) / \mu \tag{13}$$

Permeability parameters applying Darcy's law are shown in Fig. 11. Both the weight method and the time method applied showed similar results with very small standard deviation (SD). Mean permeability versus mean scaffold porosity graph showed that increases in permeability depend not only on porosity but on pore size (Fig. 12). For example, the porosity of SG80 was slightly higher than that of SNG, but the permeability values of these same scaffolds were almost double. This might be due to the large difference in pore size (3 mm vs. 0.98 mm). t-test between drilled and non-drilled structures show no significant difference neither in K_D or K^*_D for the three comparisons (SG65 vs. SG65D, SG70 vs. SG70D, and SG80 vs. SG80D). Darcian and non-Darcian permeability parameters derived from Forchheimer's law showed that there is not a direct correlation between such parameters (Fig. 13).

4. Discussion

In the present study, different metallic biomaterial scaffolds orientated to bone defect reconstruction have been designed and fabricated
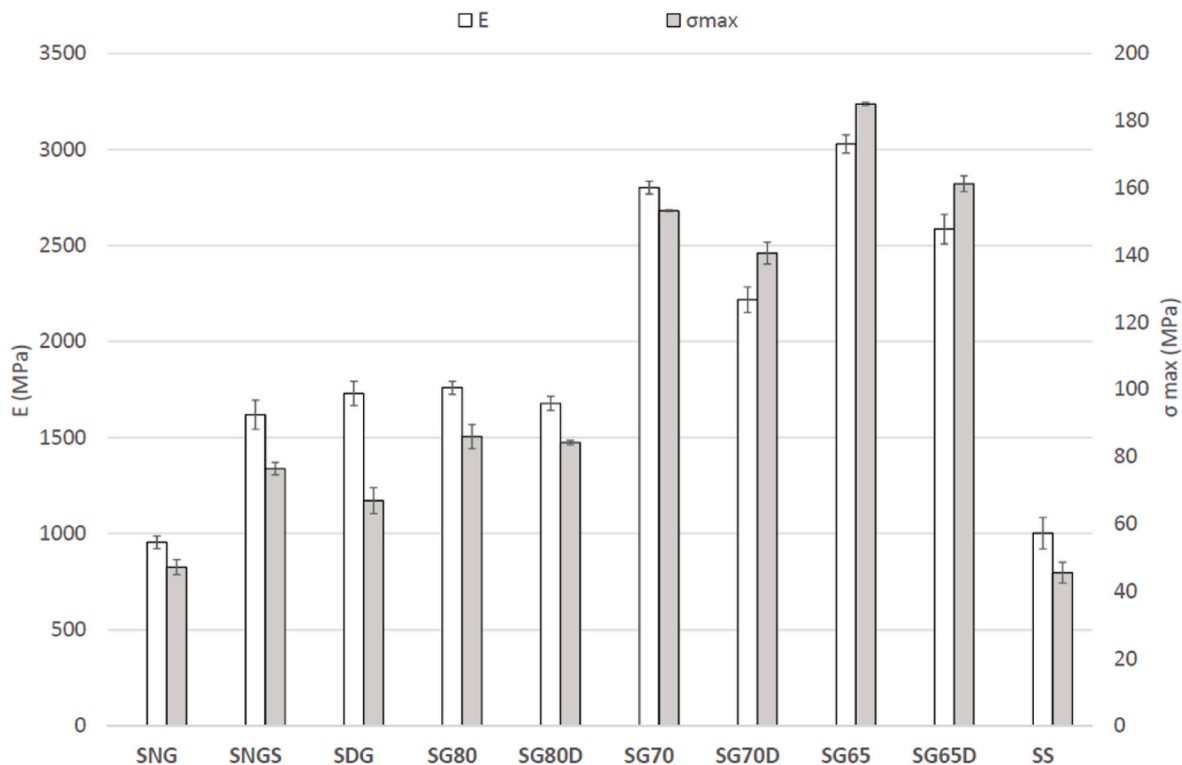
Fig. 7. Apparent Young's modulus (E_{ap}) and ultimate strength (σ_{max}) (means and standard deviations) obtained from the uniaxial compression tests.
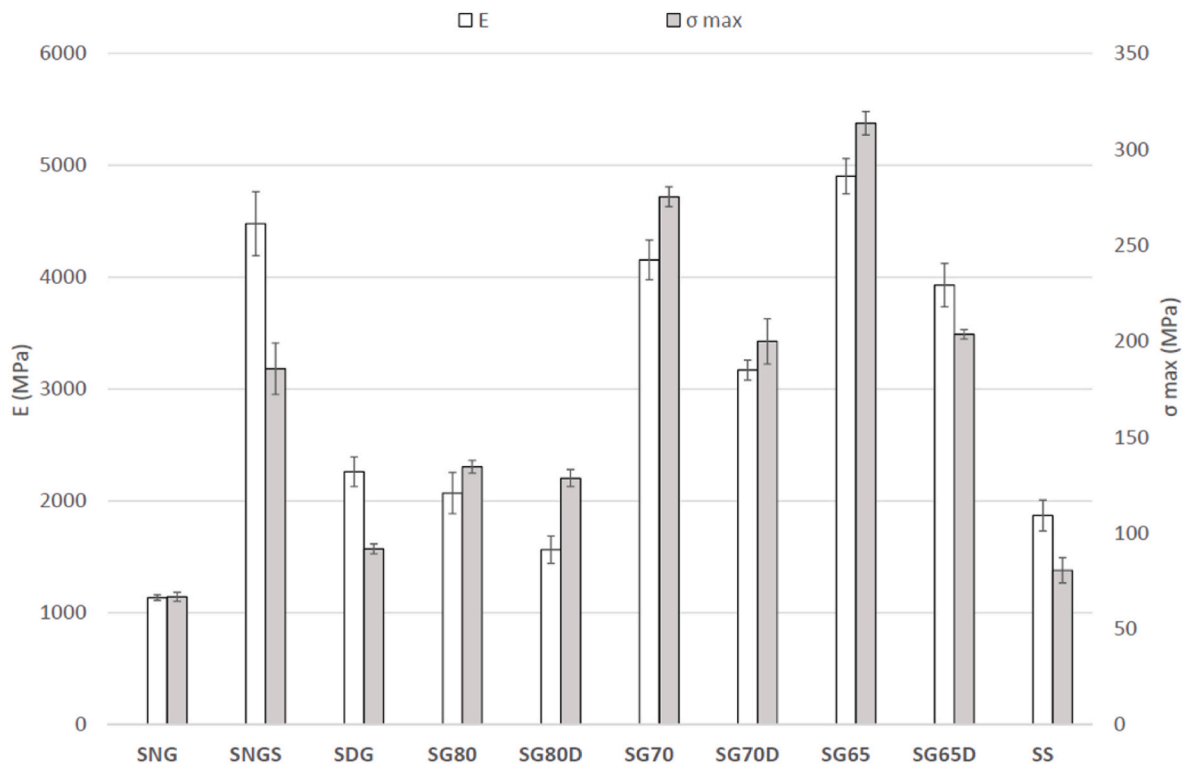

Fig. 8. Apparent bending modulus and bending strength (mean and standard deviation) obtained from the bending tests.

by LPBF. Then, the mechanical behaviour of them, in terms of compression, bending, and torsion mechanical properties, were characterized. The permeability of all the scaffolds was also analysed.

4.1. Scaffold morphology

Regarding the morphology of the bone scaffolds, there are three aspects that greatly determine their success: porosity, pore size and typology [30]. Perier-Metz et al., 2021 [31] investigated *in-silico* the
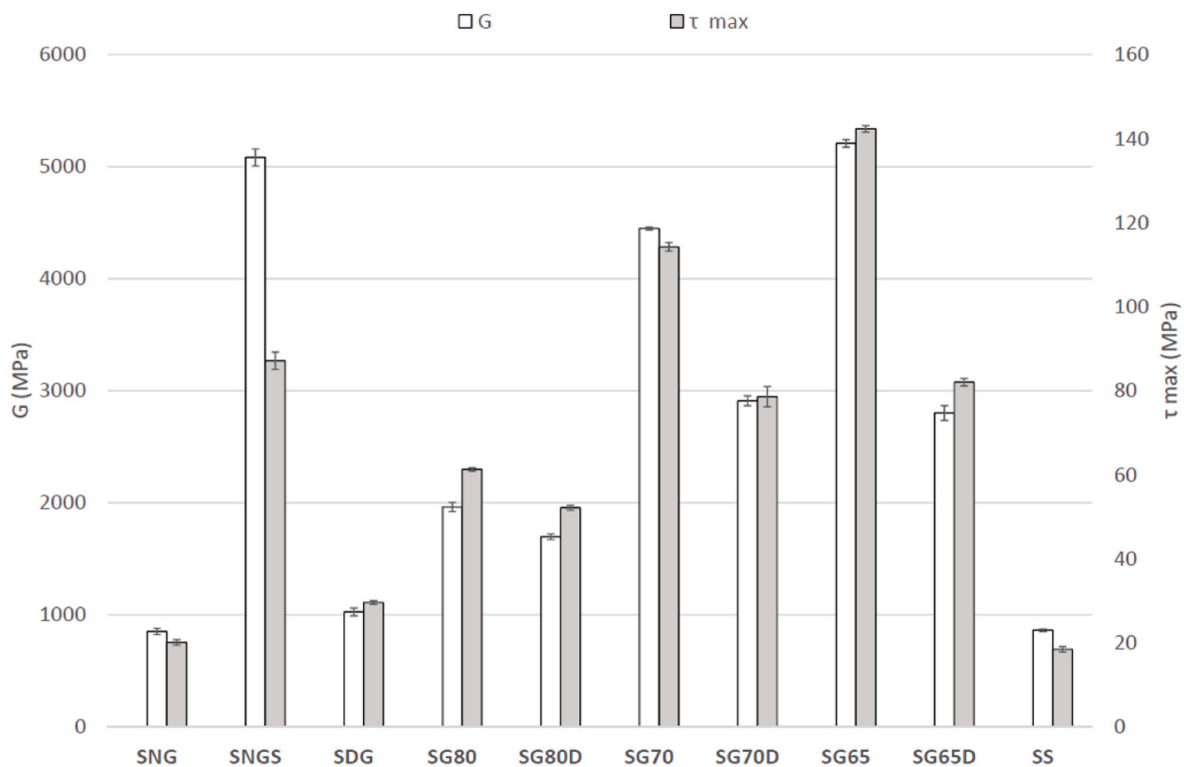
Fig. 9. Apparent shear modulus and shear strength (mean and standard deviation) obtained from the torsion tests.

Fig. 10. Photograph of the torsional test of one of the scaffolds.

optimal mechanical conditions of scaffolds for bone regeneration and suggested that the best porosities ranged from 80 to 87 %. Porosities over 90 % showed impaired healing. The porosity of human trabecular bone is in the range of 70 % and 90 %, which might be the optimal porosity for porous scaffolds [32]. In the present study, the scaffolds porosities were around 80 %, except for sheet gyroid 70, sheet gyroid 65, sheet gyroid 70 drilled, and sheet gyroid 65 drilled, which, due to the need to reduce the pore size to around 1 mm, the porosities were below 72 %. In future studies, the analysis of other porosities could be considered.

Pore size is one of the most influential morphological parameters in the proliferation and differentiation of osteoblasts on porous scaffolds [33]. There is great controversy in identifying the optimal pore size for bone cell proliferation. Different *in vitro*, *in vivo* and *in silico* studies have reached contrasting conclusions. Li et al., 2016 [34] showed better cytocompatibility and favourable bone ingrowth in porous Ti-6Al-4V scaffolds with pore size of 300–400 μm than in scaffolds with pore size of 400–700 μm. However, Bael et al., 2012 [35] showed better cell density and metabolic activity on titanium scaffolds with pore size of 1000 μm than ones with pore size of 500 μm. In their *in-silico* study, Perier-Metz et al., 2022 [36] predicted that the highest volume fraction

of regenerated bone corresponded to pore sizes between 700 μm and 800 μm. Wang et al., 2021 [33] suggested that porous Ti-6Al-4V scaffolds with a design pore size of 1000 μm can better promote the adhesion, proliferation, and osteogenic differentiation of bone marrow mesenchymal stem cells. Other authors reported that bone ingrowth was possible even with a pore size of up to 1200 μm [32]. In any case, the pore size of porous scaffolds can range from 300 to 1200 μm to promote bone cell proliferation. In the present study, the design of scaffolds with pore sizes close to 1000 μm was proposed. Scaffold pore size measurements ranged from 960 to 1050 μm, except for sheet gyroid 80 and sheet gyroid 80 drilled, whose pore sizes were around 3000 μm. The pore size of the fabricated scaffolds is usually smaller than the pore size designed in the CAD [33,37].

By tuning the manufacturing parameters such as pore shape, porosity, and pore size of TPMS structures, it could be possible to obtain scaffolds with optimal bone tissue regeneration results [30]. As in trabecular bone, the mean curvature of TPMS structures is close to zero [38]. However, TPMS structures are much more isotropic than trabecular bone tissue, and the consequences derived from this difference in the bone tissue regeneration process are difficult to predict [17]. In this work, those stochastic structures that possessed an anisotropy much higher than the TPMS structures were also analysed. However, they did not present a mean curvature close to zero and they did not show very encouraging mechanical properties.

4.2. Influence of mechanical properties on bone growth

One of the parameters that decisively determine the adequate bone growth inside the scaffolds in large bone defects is the apparent strain. The apparent strain in the range of 0.23–0.6 % seems beneficial for endochondral and intramembranous ossification [39]. Recently *in vivo* studies in sheep confirm the idea that more strains mean more bone formation [40,41]. Low strains could lead to the stress shielding phenomenon and, consequently, could promote bone resorption and implant failure [42]. To achieve sufficient strains and avoid stress shielding, the scaffold cannot be too stiff. In this sense, a balance must be
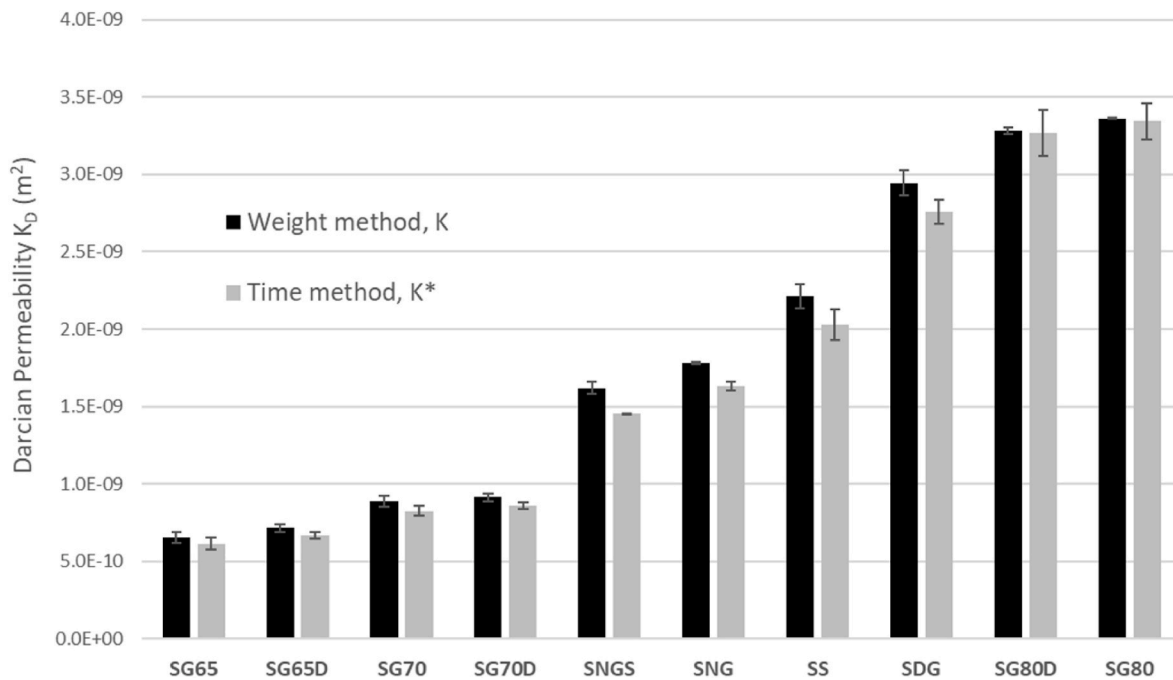
Fig. 11. Diagram showing K_D and K^*_D (mean and SD) for all the tested scaffolds.
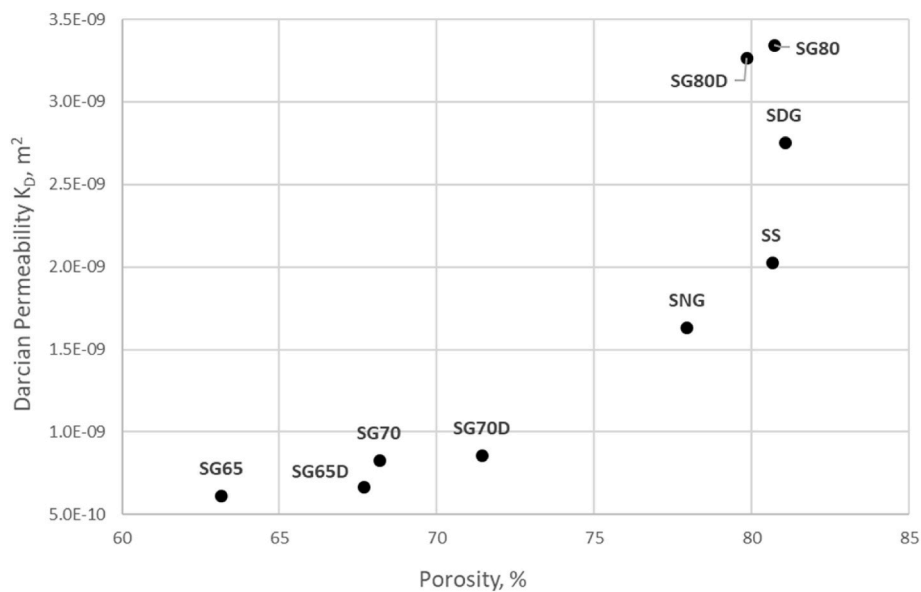

Fig. 12. Mean permeability vs. mean scaffolds porosity.

sought between adequate stiffness and high strength, which is difficult to achieve. The elastic modulus of the scaffold should be in the range of human trabecular bone (between 0.05 and 3.2 GPa) [43,44]. Some *in vivo* studies showed that scaffolds with an apparent Young's modulus greater than 2 GPa achieve less bone regeneration [39,40]. Some authors even suggest that softer scaffolds (with apparent Young's modulus lower than 1 GPa) might be more beneficial for bone tissue regeneration [31,39,45]. In the present study, the skeletal gyroid scaffolds, the stochastic and the sheet gyroid 80 (drilled and non-drilled) maintained an E_{ap} below 2 GPa and only the skeletal normal gyroid was below 1 GPa. The sheet gyroid 65 and the sheet gyroid 70 (drilled and non-drilled) were a bit stiffer in compression.

With some manufacturing technologies and materials, some of those used in this work, the reduction in the wall thickness of the sheet gyroid

scaffolds does not guarantee the continuity of the sheets or their mechanical resistance. However, in other studies using EBM technology [46,47] or other materials such as 316 L stainless steel [48], the wall thicknesses obtained was lower than that in this study for sheet-based TPMS scaffolds. In scaffolds with very large wall thicknesses (>0.3 mm), it is necessary to excessively increase the pore size (greater than the size recommended for cell growth) if one wishes to adequately reduce the stiffness. In this case, one option could be to obtain large pores and fill them with some type of material that could promote cell growth such as, among others, silicon substituted hydroxyapatite vascular endothelial growth factor (VEGF), autologous cancellous bone graft (ABG) [39,49]. Drilled sheet gyroid scaffolds showed lower stiffness values compared to their non-drilled versions. This could be an advantage as changing the diameter of the holes drilled in their walls
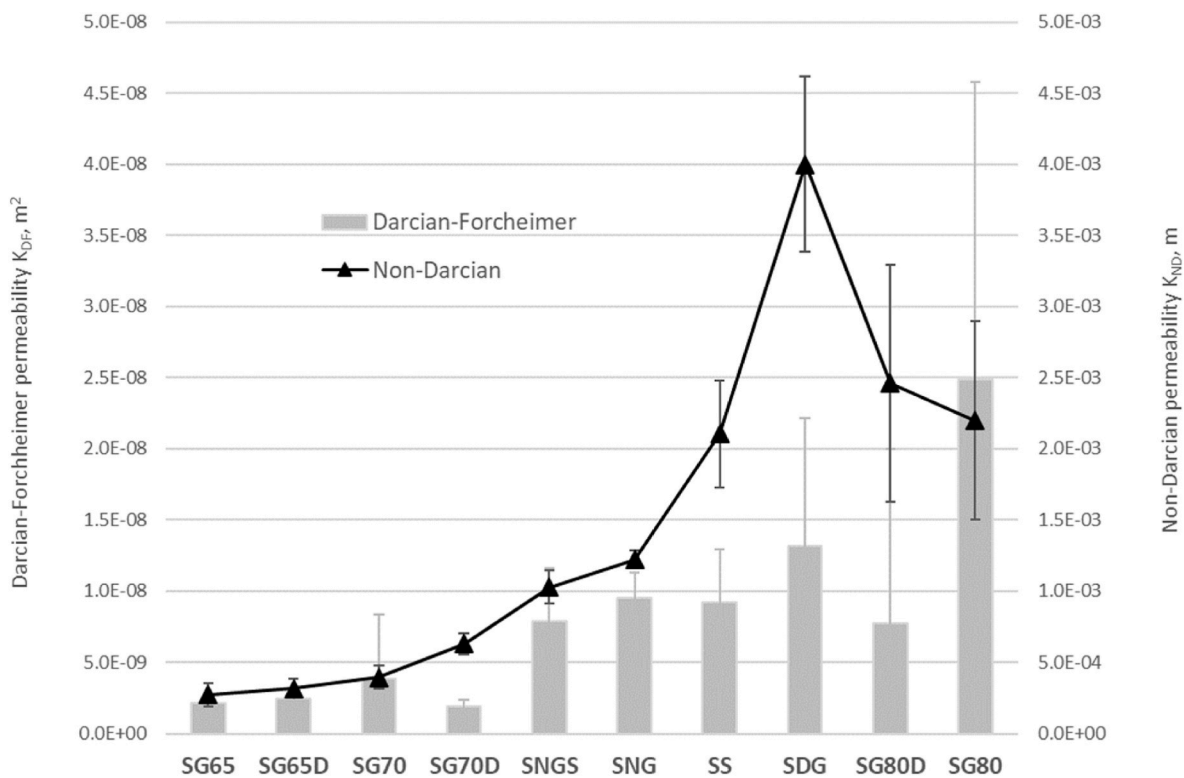
Fig. 13. Diagram showing K_{DF} and K_{ND} (mean and SD) for different scaffolds.

could be a solution to adjust the stiffness of the scaffolds and improve bidirectional permeability. However, it must be taken into account that the strength would be also affected, so more biomechanical studies would be necessary.

Regarding the scaffold strength, this must be high enough so that collapse does not occur. Therefore, its ultimate stress should fall within the range of cortical bone (between 107 and 215 MPa) [50]. In this study, only the Sheet Gyroid 65 and the Sheet Gyroid 70 (drilled and non-drilled) were in that range. However, in large bone defects, scaffolds should be accompanied by an internal fixation system, such as an osteosynthesis plate with cortical screws; thus, the physiological loads are distributed between the scaffold and the fixation system [6,34]. In the future, it would be interesting to carry out more studies on the stiffness and the strength of scaffolds and on internal fixation combinations.

The percentage differences in the values of bending properties among all the scaffolds were similar to those showed in compression. However, the stiffness and strength values (E_{ap} and σ_{max}) were higher than those obtained in compression tests, as in the study of Chen et al., 2022 [51], where both compression and flexion tests were carried out. Therefore, scaffolds can behave more securely under bending loads than under compressive loads. However, it would be advisable to carry out fatigue studies.

Torsional stiffness values of all the scaffolds in this study were higher than the values of trabecular bone (289 ± 140 MPa) [52], and lower than the values of cortical bone (3300 ± 400 MPa) [1]. Regarding torsional strength values, in all scaffolds, they were close to or even exceeded the values of cortical bone (65 ± 4 MPa) [1] except for Skeletal Normal Gyroid, Skeletal Deformed Gyroid, and Stochastic Structures. These last two mentioned structures showed poor torsional properties. The lack of torsional strength of Skeletal Normal Gyroid structures can be compensated with the internal fixation system that must accompany the scaffold in its initial stages, until there is an increase in strength provided by cell growth itself, as explained in compression. In the case of gyroid sheet scaffolds, a much more evident percentage decrease in

torsion properties compared to compression properties was detected when drilling a hole in the scaffold walls.

4.3. Scaffold permeability

Table 4 shows the permeability values obtained by other authors in experimental testing. Reported values have a 4th order of magnitude difference among them (1.63×10^{-11} m^2 to 1.20×10^{-7} m^2). This results dispersion could be attributed to two factors: the porosity and the permeability testing protocol. Thus, e.g., using the same protocol, Bobbert et al. [17] obtained permeability more than 100 times greater when porosity varied from 43 % to 77 %. On the other hand, researchers that applied a pump to achieve a controlled constant flow rate as an experimental setup [28,53–55] obtained significantly higher permeability values than the authors who used the falling head method [56–58], as it is the case in the present study. Other methods, such as using constant flow rate, but with air as fluid [7,59], showed values comparable to this study. Therefore, it is recommended to compare

Table 4
Permeability values obtained by other researchers.

Author	Ref.	Permeability K_D ($\times 10^{-10}$)	Porosity (%)
Bobbert et al., 2018	[17]	0.49–61	43–77
Castro et al., 2019	[53]	200–1200	70
Dabrowski et al., 2010	[59]	0.163–13.7	45–75
Dias et al., 2012	[9]	1.26–90.17	30–74
Lipowiecki et al., 2014	[56]	1.84–41.9	30–70
Innocentini et al., 2010	[7]	4–32.4	72–81
Montazerian et al., 2017	[62]	5–87	35–65
Ochoa et al., 2009	[63]	18.5–20.7	90–95
Pires et al., 2021	[54]	45–120	60–70
Santos et al., 2020	[28]	4.31–84.35	50–80
Timercan et al., 2021	[55]	51.5–572	60–80
Yu et al., 2020	[57]	3.0–14.8	65
Zhang et al., 2013	[64]	7.1–9.9	65
Zhang et al., 2019	[58]	0.2–4.08	10.5–91.3
Present study		6.13–33.4	65–80

permeability values using the same testing protocol. The results of K_D in this study were in the range obtained by other authors in experimental testing with the falling head method [56,57].

Previous studies have been suggested a threshold permeability value of 3×10^{-11} m^2, using the falling head method, as the required value to bone formation within the scaffold [60,61]. The results in the present study, K_D between 6.13×10^{-10} m^2 and 3.34×10^{-9} m^2, were well above that threshold, so no impediment for bone growth is expected. Moreover, the high permeability values obtained suggest that bone formation is more likely to occur than cartilage ingrowth [10,11].

As stated above, the goal of permeability calculation is to find a parameter to determine the mass transportation ability of the scaffold. In this work, the permeability coefficients K_D, K^*_D, K_{DF} y K_{ND} described in equations (7)–(9) were obtained. The values of both K_D and K^*_D for each scaffold have a negligible SD, showing the repeatability and reliability of these permeability measurement in highly porous TPMS metallic scaffolds. K_D and K^*_D are very similar between them for each scaffold (differences of less than 10 % in all cases), so both are equivalent parameters to define permeability. Although Forchheimer's law fits the experimental data better than a linear regression (Fig. 6), a small variation of the parabola in the analysed interval causes the best-fit coefficients to vary enormously. That is, the coefficients of the Forchheimmer equation are extremely sensitive to very small variations in the curve. K_{DF} and K_{ND} have a much higher SD (Fig. 13) and are not correlated to K_D or K^*_D, so their interpretation may not be straightforward. Moreover, having two parameters (K_{DF} and K_{ND}) to describe one single property, i.e., permeability, may be cumbersome. On the contrary, the only linear coefficient of the Darcy equation is very stable for small differences in the curve. These results suggest, in addition to the notion that the exact value of the permeability is not essential, that K_D (or K^*_D) should be used as the only permeability parameter, rather than the two parameters of Forchheimer's law. This is in line with the ASTM standard guide for determining the mean Darcy permeability coefficient for a porous tissue scaffold [65] that accepts the determination of Darcy permeability coefficient based in non-linear plots.

The more the permeability, the more the mass transport capacity, and therefore more facility for cell bone proliferation is expected, as long as the pore size is suitable for bone cells growth. In this study, the highest permeability K_D was obtained for the SG80 and the SG80D structures. For the ~ 1 mm pore size scaffolds, the highest porosity was reached in the SDG structures so, if only mass transport capacity for cell growth is considered, this scaffold typology seems to be the most adequate. However, mechanical stimulus is another important factor to cell proliferation, so a trade-off between permeability and stiffness should be reached for an optimal scaffold design.

In line with other research studies [9,17], the results of this work showed that the more the porosity, the higher the permeability. Drilling the sheet scaffolds does not significantly increase permeability, at least in the present mono-dimensional way to measure it. Likely, by applying a technique to measure radial permeability [62], a difference in permeability between drilled and non-drilled scaffolds may be detected.

4.4. Limitations

With porous structures obtained by additive manufacturing (LPBF) and aimed at bone tissue regeneration, cyclic loads largely determine the success of the scaffolds. Therefore, in the future, it would be necessary to carry out fatigue tests. In this study, only vertical permeability assays were considered. However, transverse permeability can influence and condition suitable bone tissue growth. Finally, to reinforce the hypotheses and conclusions of this study, it would be necessary to carry out biological assays (*in vitro* or/and *in vivo*) in future works.

5. Conclusions

Based on a review of different research studies that highlight the most optimal characteristics of typology, porosity and pore size of scaffolds aimed at the reconstruction of large bone defects, TPMS titanium scaffolds fabricated by LBPF (skeletal gyroids and sheet gyroids with porosities between 65 % and 80 %, and pore size close to 1 mm) have been investigated. The results are summarized as follows.

1. According to the literature, strain is one of the parameters determining the correct cell growth inside the scaffold. This property must be high enough and therefore the scaffold must not be excessively stiff. Some authors point out that Young's modulus should be lower than 2 GPa, or even better, below 1 GPa. In this study, compression tests showed that the skeletal gyroid scaffolds maintained an E_{ap} below 2 GPa. Only the Skeletal Normal Gyroid scaffolds ranged below 1 GPa. Sheet gyroid scaffolds could be too stiff to promote optimal bone growth inside the scaffold. However, using other biomaterials and manufacturing technologies less stiff sheet-TPMS scaffolds could be obtained.
2. Compression tests also showed that only the Sheet Gyroid 65 and Sheet Gyroid 70 (drilled and non-drilled) scaffolds were in the cortical bone strength range. Therefore, for the rest of the scaffolds, it is recommended to add an osteosynthesis plate with cortical screws to distribute the loads.
3. Percentage differences among the scaffolds in the bending properties were similar to those obtained in compression, although the values of stiffness and strength were higher in bending.
4. The torsional properties of the scaffolds in this study were acceptable for bone defect repairs, except for the Skeletal Deformed Gyroid and the Stochastic Structures, which showed very poor torsional features.
5. The permeability coefficient derived from Darcy's law (ranging from 6.13×10^{-10} m^2 to 3.34×10^{-9} m^2) was shown to be a reliable measure of permeability in TPMS metal scaffolds. However, the two permeability parameters derived from Forchheimer's law were difficult to interpret due to their high variability and lack of correlation between them.

CRediT authorship contribution statement

Alejandro Yánez: Writing – original draft, Supervision, Project administration, Methodology, Investigation, Funding acquisition, Conceptualization. **Alberto Cuadrado:** Validation, Software, Methodology, Investigation, Data curation. **Oscar Martel:** Writing – review & editing, Supervision, Investigation, Formal analysis. **María Paula Fiorucci:** Investigation, Formal analysis, Data curation. **Sebastiaan Deviaene:** Software, Formal analysis, Data curation, Conceptualization.

Declaration of competing interest

The authors declare that they have no known competing financial interests or personal relationships that could have appeared to influence the work reported in this paper.

Data availability

Data will be made available on request.

Acknowledgements

References

[1] X. Wang, S. Xu, S. Zhou, W. Xu, M. Leary, P. Choong, M. Qian, M. Brandt, Y.M. Xie, Topological design and additive manufacturing of porous metals for bone scaffolds and orthopaedic implants: a review, Biomaterials 83 (2016) 127–141, https://doi.org/10.1016/j.biomaterials.2016.01.012.

[2] S.M. Ahmadi, R. Hedayati, Y. Li, K. Lietaert, N. Tümer, A. Fatemi, C.D. Rans, B. Pouran, H. Weinans, A.A. Zadpoor, Fatigue performance of additively manufactured meta-biomaterials: the effects of topology and material type, Acta Biomater. 65 (2018) 292–304, https://doi.org/10.1016/j.actbio.2017.11.014.

[3] X.P. Tan, Y.J. Tan, C.S.L. Chow, S.B. Tor, W.Y. Yeong, Metallic powder-bed based 3D printing of cellular scaffolds for orthopaedic implants : a state-of-the-art review on manufacturing , topological design , mechanical properties and biocompatibility, Mater. Sci. Eng. C 76 (2017) 1328–1343, https://doi.org/10.1016/j.msec.2017.02.094.

[4] S.L. Sing, J. An, W.Y. Yeong, F.E. Wiria, Laser and electron-beam powder-bed additive manufacturing of metallic implants: a review on processes, materials and designs, J. Orthop. Res. 34 (2016) 369–385, https://doi.org/10.1002/jor.23075.

[5] S.A. Naghavi, M. Tamaddon, A. Marghoub, K. Wang, B.B. Babamiri, K. Hazeli, W. Xu, X. Lu, C. Sun, L. Wang, M. Moazen, L. Wang, D. Li, C. Liu, Mechanical characterisation and numerical modelling of TPMS-based gyroid and diamond Ti6Al4V scaffolds for bone implants: an integrated approach for translational consideration, Bioengineering 9 (2022) 154–162, https://doi.org/10.3390/bioengineering9100504.

[6] A. Yánez, A. Cuadrado, O. Martel, H. Afonso, D. Monopoli, Gyroid porous titanium structures: a versatile solution to be used as scaffolds in bone defect reconstruction, Mater. Des. 140 (2018), https://doi.org/10.1016/j.matdes.2017.11.050.

[7] M.D.M. Innocentini, R.K. Faleiros, R. Pisani, I. Thijs, J. Luyten, S. Mullens, Permeability of porous gelcast scaffolds for bone tissue engineering, J. Porous Mater. 17 (2010) 615–627, https://doi.org/10.1007/s10934-009-9331-2.

[8] A.G. Mitsak, J.M. Kemppainen, M.T. Harris, S.J. Hollister, Effect of polycaprolactone scaffold permeability on bone regeneration in vivo, Tissue Eng. 17 (2011) 1831–1839, https://doi.org/10.1089/ten.tea.2010.0560.

[9] M.R. Dias, P.R. Fernandes, J.M. Guedes, S.J. Hollister, Permeability analysis of scaffolds for bone tissue engineering, J. Biomech. 45 (2012) 938–944, https://doi.org/10.1016/j.jbiomech.2012.01.019.

[10] J.M. Kemppainen, S.J. Hollister, Differential effects of designed scaffold permeability on chondrogenesis by chondrocytes and bone marrow stromal cells, Biomaterials 31 (2010) 279–287, https://doi.org/10.1016/j.biomaterials.2009.09.041.

[11] C.G. Jeong, H. Zhang, S.J. Hollister, Three-dimensional poly(1,8-octanediol-co-citrate) scaffold pore shape and permeability effects on sub-cutaneous in vivo chondrogenesis using primary chondrocytes, Acta Biomater. 7 (2011) 505–514, https://doi.org/10.1016/j.actbio.2010.08.027.

[12] O. Al-Ketan, R. Rowshan, R.K. Abu Al-Rub, Topology-mechanical property relationship of 3D printed strut, skeletal, and sheet based periodic metallic cellular materials, Addit. Manuf. 19 (2018) 167–183, https://doi.org/10.1016/j.addma.2017.12.006.

[13] J. Jin, S. Wu, L. Yang, C. Zhang, Y. Li, C. Cai, C. Yan, Y. Shi, Ni–Ti multicell interlacing Gyroid lattice structures with ultra-high hyperelastic response fabricated by laser powder bed fusion, Int. J. Mach. Tool Manufact. 195 (2024) 104099, https://doi.org/10.1016/j.ijmachtools.2023.104099.

[14] X. Guo, J. Ding, X. Li, S. Qu, J.Y. Hsi Fuh, W.F. Lu, X. Song, W. Zhai, Interpenetrating phase composites with 3D printed triply periodic minimal surface (TPMS) lattice structures, Composites, Part B 248 (2023) 110351, https://doi.org/10.1016/j.compositesb.2022.110351.

[15] C. Zhang, H. Qiao, L. Yang, W. Ouyang, T. He, B. Liu, X. Chen, N. Wang, C. Yan, Vibration characteristics of additive manufactured IWP-type TPMS lattice structures, Compos. Struct. 327 (2024) 117642, https://doi.org/10.1016/j.compstruct.2023.117642.

[16] E. Yang, M. Leary, B. Lozanovski, D. Downing, M. Mazur, A. Sarker, A. Khorasani, A. Jones, T. Maconachie, S. Bateman, M. Easton, M. Qian, P. Choong, M. Brandt, Effect of geometry on the mechanical properties of Ti-6Al-4V Gyroid structures fabricated via SLM: a numerical study, Mater. Des. (2019) 108165, https://doi.org/10.1016/J.MATDES.2019.108165.

[17] F.S.L. Bobbert, K. Lietaert, A.A. Eftekhari, B. Pouran, S.M. Ahmadi, H. Weinans, A.A. Zadpoor, Additively manufactured metallic porous biomaterials based on minimal surfaces: a unique combination of topological, mechanical, and mass transport properties, Acta Biomater. 53 (2017) 572–584, https://doi.org/10.1016/j.actbio.2017.02.024.

[18] S. AlMahri, R. Santiago, D.W. Lee, H. Ramos, H. Alabdouli, M. Alteneiji, Z. Guan, W. Cantwell, M. Alves, Evaluation of the dynamic response of triply periodic minimal surfaces subjected to high strain-rate compression, Addit. Manuf. 46 (2021) 102220, https://doi.org/10.1016/j.addma.2021.102220.

[19] P. Hameed, C.F. Liu, R. Ummethala, N. Singh, H.H. Huang, G. Manivasagam, K.G. Prashanth, Biomorphic porous Ti6Al4V gyroid scaffolds for bone implant applications fabricated by selective laser melting, Prog. Addit. Manuf. 6 (2021) 455–469, https://doi.org/10.1007/s40964-021-00210-5.

[20] F. Liu, Q. Ran, M. Zhao, T. Zhang, D.Z. Zhang, Z. Su, Additively manufactured continuous cell-size gradient porous scaffolds: pore characteristics, mechanical properties and biological responses in vitro, Materials 13 (2020), https://doi.org/10.3390/ma13112589.

[21] K. Yeranee, Y. Rao, A review of recent investigations on flow and heat transfer enhancement in cooling channels embedded with triply periodic minimal surfaces (TPMS), Energies 15 (2022), https://doi.org/10.3390/en15238994.

[22] M. Speirs, B. Van Hooreweder, J. Van Humbeeck, J.P. Kruth, Fatigue behaviour of NiTi shape memory alloy scaffolds produced by SLM, a unit cell design comparison, J. Mech. Behav. Biomed. Mater. 70 (2017) 53–59, https://doi.org/10.1016/j.jmbbm.2017.01.016.

[23] International Organization for Standardization, ISO 13314:2011 Mechanical testing of metals – ductility testing – compression test for porous and cellular metals (ISO Standard No. 13314:2011(E)), Int. Organ. Stand. 2011 (2011).

[24] ASTM, ASTM, C1674 - 11 standard test method for flexural strength of advanced ceramics with engineered porosity (honeycomb cellular channels) at ambient temperatures, Annu. Book ASTM Stand. i (2015).

[25] ASTM standard E28, Standard Test Method for Shear Modulus at Room Temperature, E1vols. 43–20, Astm, 1987, p. 87.

[26] D. Lasseux, F.J. Valdés-Parada, On the developments of Darcy's law to include inertial and slip effects, Compt. Rendus Mec. 345 (2017) 660–669, https://doi.org/10.1016/j.crme.2017.06.005.

[27] J.F. Despois, A. Mortensen, Permeability of open-pore microcellular materials, Acta Mater. 53 (2005) 1381–1388, https://doi.org/10.1016/j.actamat.2004.11.031.

[28] J. Santos, T. Pires, B.P. Gouveia, A.P.G. Castro, P.R. Fernandes, On the permeability of TPMS scaffolds, J. Mech. Behav. Biomed. Mater. 110 (2020) 1–7, https://doi.org/10.1016/j.jmbbm.2020.103932.

[29] F. Pennella, G. Cerino, D. Massai, D. Gallo, G. Falvo D'Urso Labate, A. Schiavi, M.A. Deriu, A. Audenino, U. Morbiducci, A survey of methods for the evaluation of tissue engineering scaffold permeability, Ann. Biomed. Eng. 41 (2013) 2027–2041, https://doi.org/10.1007/s10439-013-0815-5.

[30] Z. Dong, X. Zhao, Application of TPMS structure in bone regeneration, Eng. Regen. 2 (2021) 154–162, https://doi.org/10.1016/j.engreg.2021.09.004.

[31] C. Perier-Metz, G.N. Duda, S. Checa, Initial mechanical conditions within an optimized bone scaffold do not ensure bone regeneration – an in silico analysis, Biomech. Model. Mechanobiol. 20 (2021) 1723–1731, https://doi.org/10.1007/s10237-021-01472-2.

[32] Z. Wang, C. Li, Y. Qin, L. Zhong, B. Chen, Z. Li, H. Liu, F. Chang, J. Wang, Analysis of factors influencing bone ingrowth into three-dimensional printed porous metal scaffolds: a review, J. Alloys Compd. 717 (2017) 271–285, https://doi.org/10.1016/j.jallcom.2017.05.079.

[33] C. Wang, D. Xu, L. Lin, S. Li, W. Hou, Y. He, L. Sheng, C. Yi, X. Zhang, H. Li, Y. Li, W. Zhao, D. Yu, Large-pore-size Ti6Al4V scaffolds with different pore structures for vascularized bone regeneration, Mater. Sci. Eng. C 131 (2021), https://doi.org/10.1016/j.msec.2021.112499.

[34] G. Li, L. Wang, W. Pan, F. Yang, W. Jiang, X. Wu, X. Kong, K. Dai, Y. Hao, In vitro and in vivo study of additive manufactured porous Ti6Al4V scaffolds for repairing bone defects, Sci. Rep. 6 (2016) 1–11, https://doi.org/10.1038/srep34072.

[35] S. Van Bael, Y.C. Chai, S. Truscello, M. Moesen, G. Kerckhofs, H. Van Oosterwyck, J.P. Kruth, J. Schrooten, The effect of pore geometry on the in vitro biological behavior of human periosteum-derived cells seeded on selective laser-melted Ti6Al4V bone scaffolds, Acta Biomater. 8 (2012) 2824–2834, https://doi.org/10.1016/j.actbio.2012.04.001.

[36] C. Perier-Metz, A. Cipitria, D.W. Hutmacher, G.N. Duda, S. Checa, An in silico model predicts the impact of scaffold design in large bone defect regeneration, Acta Biomater. 145 (2022) 329–341, https://doi.org/10.1016/j.actbio.2022.04.008.

[37] Q. Ran, W. Yang, Y. Hu, X. Shen, Y. Yu, Y. Xiang, K. Cai, Osteogenesis of 3D printed porous Ti6Al4V implants with different pore sizes, J. Mech. Behav. Biomed. Mater. 84 (2018) 1–11, https://doi.org/10.1016/j.jmbbm.2018.04.010.

[38] H. Jinnai, H. Watashiba, T. Kajihara, Y. Nishikawa, M. Takahashi, M. Ito, Surface curvatures of trabecular bone microarchitecture, Bone 30 (2002) 191–194, https://doi.org/10.1016/S8756-3282(01)00672-X.

[39] A.-M. Pobloth, S. Checa, H. Razi, A. Petersen, J.C. Weaver, K. Schmidt-Bleek, M. Windolf, A.Á. Tatai, C.P. Roth, K.-D. Schaser, G.N. Duda, P. Schwabe, Mechanobiologically optimized 3D titanium-mesh scaffolds enhance bone regeneration in critical segmental defects in sheep, Sci. Transl. Med. 10 (2018) eaam8828, https://doi.org/10.1126/scitranslmed.aam8828.

[40] N. Reznikov, O.R. Boughton, S. Ghouse, A.E. Weston, L. Collinson, G.W. Blunn, J.R.T. Jeffers, J.P. Cobb, M.M. Stevens, Individual response variations in scaffold-guided bone regeneration are determined by independent strain- and injury-induced mechanisms, Biomaterials 194 (2019) 183–194, https://doi.org/10.1016/j.biomaterials.2018.11.026.

[41] A.M. Crovace, L. Lacitignola, D.M. Forleo, F. Staffieri, E. Francioso, A. Di Meo, J. Becerra, A. Crovace, L. Santos-Ruiz, 3D biomimetic porous titanium (Ti6al4v eli) scaffolds for large bone critical defect reconstruction: an experimental study in sheep, Animals 10 (2020) 1–14, https://doi.org/10.3390/ani10081389.

[42] P. Heinl, L. Müller, C. Körner, R.F. Singer, F.A. Müller, Cellular Ti-6Al-4V structures with interconnected macro porosity for bone implants fabricated by selective electron beam melting, Acta Biomater. 4 (2008) 1536–1544, https://doi.org/10.1016/j.actbio.2008.03.013.

[43] S.A. Goldstein, Goldstein J Biomech 1987.Pdf, 1987, https://doi.org/10.1016/0021-9290(87)90023-6.

[44] J. Wang, B. Zhou, X.S. Liu, A.J. Fields, A. Sanyal, X. Shi, M. Adams, T.M. Keaveny, X.E. Guo, Trabecular plates and rods determine elastic modulus and yield strength of human trabecular bone, Bone 72 (2015) 71–80, https://doi.org/10.1016/j.bone.2014.11.006.

[45] M. De Wild, C. Ghayor, S. Zimmermann, J. Rüegg, F. Nicholls, F. Schuler, T.H. Chen, F.E. Weber, Osteoconductive lattice microarchitecture for optimized bone regeneration, 3D print, Addit. Manuf. 6 (2019) 40–49, https://doi.org/10.1089/3dp.2017.0129.

[46] S. Evsevleev, T. Mishurova, D. Khrapov, A. Paveleva, D. Meinel, R. Surmenev, M. Surmeneva, A. Koptyug, G. Bruno, X-ray computed tomography procedures to quantitatively characterize the morphological features of triply periodic minimal surface structures, Materials 14 (2021), https://doi.org/10.3390/ma14113002.

[47] D. Khrapov, M. Kozadayeva, K. Manabaev, A. Panin, W. Sjöström, A. Koptyug, T. Mishurova, S. Evsevleev, D. Meinel, G. Bruno, D. Cheneler, R. Surmenev, M. Surmeneva, Different approaches for manufacturing ti-6al-4v alloy with triply periodic minimal surface sheet-based structures by electron beam melting, Materials 14 (2021), https://doi.org/10.3390/ma14174912.

[48] C. Zhang, H. Zheng, L. Yang, Y. Li, J. Jin, W. Cao, C. Yan, Y. Shi, Mechanical responses of sheet-based gyroid-type triply periodic minimal surface lattice structures fabricated using selective laser melting, Mater. Des. 214 (2022) 110407, https://doi.org/10.1016/j.matdes.2022.110407.

[49] I. Izquierdo-Barba, L. Santos-Ruiz, J. Becerra, M.J. Feito, D. Fernández-Villa, M. C. Serrano, I. Díaz-Güemes, B. Fernández-Tomé, S. Enciso, F.M. Sánchez-Margallo, D. Monopoli, H. Afonso, M.T. Portolés, D. Arcos, M. Vallet-Regí, Synergistic effect of Si-hydroxyapatite coating and VEGF adsorption on Ti6Al4V-ELI scaffolds for bone regeneration in an osteoporotic bone environment, Acta Biomater. 83 (2019) 456–466, https://doi.org/10.1016/j.actbio.2018.11.017.

[50] J. Wieding, A. Wolf, R. Bader, Numerical optimization of open-porous bone scaffold structures to match the elastic properties of human cortical bone, J. Mech. Behav. Biomed. Mater. 37 (2014) 56–68, https://doi.org/10.1016/j.jmbbm.2014.05.002.

[51] X. Chen, Y. Wu, H. Liu, Y. Wang, G. Zhao, Q. Zhang, F. Wang, Y. Liu, Mechanical performance of PEEK-Ti6Al4V interpenetrating phase composites fabricated by powder bed fusion and vacuum infiltration targeting large and load-bearing implants, Mater. Des. 215 (2022) 110531, https://doi.org/10.1016/j.matdes.2022.110531.

[52] K. Bruyère Garnier, R. Dumas, C. Rumelhart, M.E. Arlot, Mechanical characterization in shear of human femoral cancellous bone: torsion and shear tests, Med. Eng. Phys. 21 (1999) 641–649, https://doi.org/10.1016/S1350-4533(99)00096-X.

[53] A.P.G. Castro, T. Pires, J.E. Santos, B.P. Gouveia, P.R. Fernandes, Permeability versus design in TPMS scaffolds, Materials 12 (2019), https://doi.org/10.3390/ma12081313.

[54] T. Pires, J. Santos, R.B. Ruben, B.P. Gouveia, A.P.G. Castro, P.R. Fernandes, Numerical-experimental analysis of the permeability-porosity relationship in triply periodic minimal surfaces scaffolds, J. Biomech. 117 (2021) 110263, https://doi.org/10.1016/j.jbiomech.2021.110263.

[55] A. Timercan, V. Sheremetyev, V. Brailovski, Mechanical properties and fluid permeability of gyroid and diamond lattice structures for intervertebral devices: functional requirements and comparative analysis, Sci. Technol. Adv. Mater. 22 (2021) 285–300, https://doi.org/10.1080/14686996.2021.1907222.

[56] M. Lipowiecki, M. Ryvolová, Á. Töttösi, N. Kolmer, S. Naher, S.A. Brennan, M. Vázquez, D. Brabazon, Permeability of rapid prototyped artificial bone scaffold structures, J. Biomed. Mater. Res., Part A 102 (2014) 4127–4135, https://doi.org/10.1002/jbm.a.35084.

[57] G. Yu, Z. Li, S. Li, Q. Zhang, Y. Hua, H. Liu, X. Zhao, D.T. Dhaidhai, W. Li, X. Wang, The select of internal architecture for porous Ti alloy scaffold: a compromise between mechanical properties and permeability, Mater. Des. 192 (2020) 108754, https://doi.org/10.1016/j.matdes.2020.108754.

[58] X.Y. Zhang, G. Fang, S. Leeflang, A.A. Zadpoor, J. Zhou, Topological design, permeability and mechanical behavior of additively manufactured functionally graded porous metallic biomaterials, Acta Biomater. 84 (2019) 437–452, https://doi.org/10.1016/j.actbio.2018.12.013.

[59] B. Dabrowski, W. Swieszkowski, D. Godlinski, K.J. Kurzydlowski, Highly porous titanium scaffolds for orthopaedic applications, J. Biomed. Mater. Res. Part B Appl. Biomater. 95 (2010) 53–61, https://doi.org/10.1002/jbm.b.31682.

[60] A.C. Jones, C.H. Arns, D.W. Hutmacher, B.K. Milthorpe, A.P. Sheppard, M. A. Knackstedt, The correlation of pore morphology, interconnectivity and physical properties of 3D ceramic scaffolds with bone ingrowth, Biomaterials 30 (2009) 1440–1451, https://doi.org/10.1016/j.biomaterials.2008.10.056.

[61] P.W. Hui, P.C. Lmng, A. Sher, Technical Note Bone Graft as a Predictor Healing, 1994.

[62] H. Montazerian, M. Zhianmanesh, E. Davoodi, A.S. Milani, M. Hoorfar, Longitudinal and radial permeability analysis of additively manufactured porous scaffolds: effect of pore shape and porosity, Mater. Des. 122 (2017) 146–156, https://doi.org/10.1016/j.matdes.2017.03.006.

[63] I. Ochoa, J.A. Sanz-Herrera, J.M. García-Aznar, M. Doblaré, D.M. Yunos, A. R. Boccaccini, Permeability evaluation of 45S5 Bioglass®-based scaffolds for bone tissue engineering, J. Biomech. 42 (2009) 257–260, https://doi.org/10.1016/j.jbiomech.2008.10.030.

[64] Z. Zhang, D. Jones, S. Yue, P.D. Lee, J.R. Jones, C.J. Sutcliffe, E. Jones, Hierarchical tailoring of strut architecture to control permeability of additive manufactured titanium implants, Mater. Sci. Eng. C 33 (2013) 4055–4062, https://doi.org/10.1016/j.msec.2013.05.050.

[65] ASTM, Standard Guide for Determining the Mean Darcy Permeability Coefficient for a Porous Tissue Scaffold, Astm, 2015.